Chiral geometric-phase metasurface for Bloch surface wave out-coupling in free space

Research Article

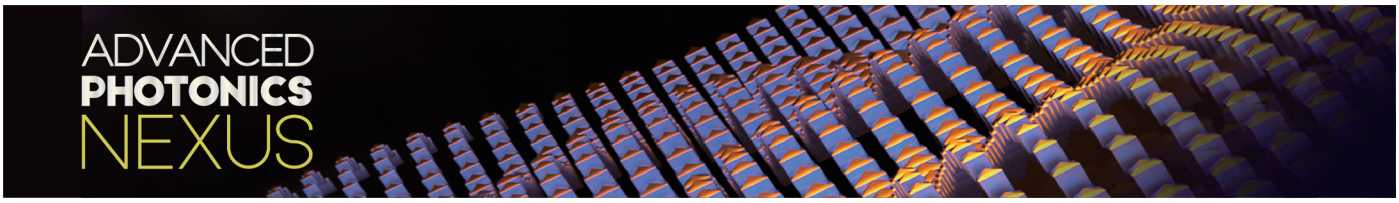

Chiral geometric-phase metasurface for Bloch surface wave out-coupling in free space

Niccolò Marcucci,[a] Zongyuan Tang,[b,c] Lilian Emonin,[d] Thierry Grosjean,[d] Yanjun Liu,[b] Matthieu Roussey,[e] Tian-Long Guo,[e,*] and Emiliano Descrovi[c]

[a]Institute of Applied Physics IFAC-CNR, Sesto Fiorentino, Italy
[b]Southern University of Science and Technology, Department of Electronic and Electrical Engineering, Shenzhen, China
[c]Politecnico di Torino, Department of Applied Science and Technology, Torino, Italy
[d]Université Marie and Louis Pasteur, FEMTO-ST Institute, Besançon, France
[e]University of Eastern Finland, Center for Photonics Sciences, Joensuu, Finland

Abstract. Vortex beams (VBs) represent an important instance of structured light carrying orbital angular momentum (OAM), which is attracting particular interest from many application fields, from free space optical communications to sensing and imaging. As OAM radiation from a single emitter is concerned, a precise positioning of the source in the center of axis-symmetric, possibly resonating diffractive structures is often required. In addition, efficient free-space outcoupling of light with pure OAM and polarization states remains a difficult task. Here, we propose a dielectric multilayer platform decorated with chiral gold metasurfaces able to provide polarization-selective diffraction of Bloch surface waves sustained by the multilayer. We demonstrate that the generation of well-defined OAM occurs only when Bloch surface waves (BSWs) are coupled (in this case, from an external coherent source). The metasurface chirality is shown to be polarization-selective so that at least 74% is out-coupled in free space with a specific circular polarization, determined by design. In perspective, this work suggests new opportunities for the generation of free-space OAM single photons as an alternative to plasmonic structures recently proposed.

Keywords: orbital angular momentum; optical vortex; chiral metasurface; Bloch surface wave.

Received Oct. 4, 2025; revised manuscript received Jan. 14, 2026; accepted for publication Jan. 19, 2026; published online Feb. 14, 2026.

[DOI: 10.1117/1.APN.5.2.026008]

1 Introduction

In a seminal work published in 1989 by Coullet et al., the concept of optical vortex appeared for the first time.[1] The underlying analogy of optical vortex with other commonly known swirling phenomena in physics relies on the topological structure of the transverse phase distribution. Vortex beams (VBs) represent a family of structured electromagnetic paraxial modes generally characterized by a phase singularity along the optical axis, surrounded by a helical wavefront. A convenient way to mathematically describe such axis-symmetric VBs is by means of Laguerre–Gauss functions, which constitute a discrete set of orthogonal modes (Hilbert basis) useful to represent any free-space propagating field. In 1992, Allen et al. demonstrated that the topological charge appearing in the Laguerre–Gauss representation of a VB unveils the existence of an orbital angular momentum (OAM) associated thereto.[2] It is now ascertained that the OAM concept can be scaled down to single photons, such that the discrete topological charge $\ell_z\hbar$ represents the eigenvalue of an OAM operator L_z for the photon. It is worth recalling that a photon also possesses a rotating electric field, resulting in a spin angular momentum (SAM) equal to $\sigma_z\hbar$, where $\sigma_z = \pm 1$ depends on its circular polarization state. Generally speaking, SAM and OAM are entangled,[3] but in the small-angle propagation limit (paraxial approximation), the two angular momenta can be handled and measured independently.[4] This means that single photons can stay in an OAM state, with a well-defined OAM value ($\ell_z\hbar$) and polarization ($\sigma_z\hbar$).

In the last 20 years, VBs have been demonstrated to provide new degrees of light-driven manipulation of micro and nanoparticles and biomolecules, to improve performances in optical microscopy and high-density optical data storage, and to

*Address all correspondence to Tian-Long Guo, tianlong.guo@uef.fi

investigate the chirality of organic molecules, which is relevant for drug discovery and therapy.[5,6] Many applications drive the demand for producing versatile and diverse devices for generating, detecting, and handling VBs. Most of the previous-art approaches for generating OAM beams in free space rely on the conversion of an incoming radiation into a specifically controlled VB. This is done with planar devices based on liquid crystals (LC) technology and anisotropic media,[7] decorated waveguides[8,9] and microdisk/microring resonators,[10,11] holographic or diffractive optical elements (DOEs), and more recently, metasurfaces (MSs).[12,13] The large majority of these solutions embody very energy-efficient mode converters.[14] The coherence properties required of a VB are inherited from the input beam, which is usually extracted from a laser source, sometimes waveguided. In an attempt to increase the level of integration, MSs or DOEs can be directly patterned on top of a vertical-cavity surface-emitting laser (VCSEL).[15]

Approaches to produce VBs based on MS or holographic/DOE are hardly suitable for single, localized sources directly integrated therein (e.g., a quantum dot, a nanowire, a lattice defect in a diamond crystal, or in a 2D semiconductor flake). In fact, since the beam conversion through DOE/MS relies on a spatial-dependent phase transformation, an emitter located in a specific position on an MS would be insensitive to the overall geometry of the MS itself, unless some collective modes are intervening.[16] This limitation becomes very relevant in cases that the outcoupled radiation from single sources is required to possess some sort of axial symmetry, as in the case of VBs. Very recently, single emitters have been coupled to surface plasmon polaritons (SPPs), which are then phase-manipulated and outcoupled in free space.[17–19] However, coupling to SPPs involves absorption losses to be considered, as well as the specific orientation of the emitter, because of the p-polarized nature of SPPs.

Here, we propose a structure based on a dielectric multilayer (or one-dimensional photonic crystal, 1DPC) patterned with chiral metasurfaces, which are demonstrated to provide outcoupled radiation by diffraction of Bloch surface waves (BSWs)[20] sustained by the multilayer. This arrangement is particularly interesting as it overcomes the limitations outlined above. In fact, if an emitter is directly positioned on the 1DPC surface, a radiation coupling effect to BSW will take place,[21–23] so that the emitted power can be diffracted in the free space in a controlled way.[24,25] The metasurface is generally composed of metallic nanorods periodically arranged in rings or spirals, with an orientation that rotates continuously along the radial direction. Although the number of spiral arms affects the OAM, the orientation of the nanorods dictates the circular polarization state of the diffracted beam. Such a polarization selectivity avoids the co-existence in the diffracted field of a pair of OAM beams with opposite helicity (SAM) and different OAM, as recently demonstrated for plasmon-coupled emission at the single photon level.[17] The use of BSW instead of surface plasmons as an intermediate energy carrier from the source to the diffracting structure allows absorption losses to be strongly reduced, if not neglected. In fact, although absorption in dielectric materials can be orders of magnitude smaller than in silver or gold (depending on the working wavelength), leakage losses (which also limit the BSW propagation length) can be further attenuated by properly designing 1DPC with a larger number of stack periods,[26] leading to propagation lengths in the centimeter scale.[27] In addition, 1DPC can be designed such that BSW with either TE-polarization (as in the present case) or TM-polarization[28–30] can be made accessible in an attempt to offer more opportunities for mode coupling with the emitter, regardless of dipole momentum orientations. In the present work, the ability of the proposed structure to produce several polarization-selective OAM beams is demonstrated using an external coherent light source as an input field to couple to BSWs.

2 Methods

2.1 Chiral Metasurface Geometry and Design

The computational model includes a dielectric multilayer, a diffractive metasurface made of gold nanoantennas, and a pair of dipole emitters. The model geometry, reference system, and notations used in this work to describe the z-components of the field's SAM and OAM are presented in Fig. 1.

The device is composed of a glass substrate supporting a dielectric stack. The alternating layers follow this order (in the positive z-direction): substrate-$[Ta_2O_5\text{-}SiO_2] \times 6$-$Ta_2O_5$-$SiO_2$-air, with 14 layers in total. The Ta_2O_5 layer (refractive index 2.08 at $\lambda = 520$ nm) is 95 nm thick, and the SiO_2 layer (refractive index 1.46 at $\lambda = 520$ nm) is 137 nm thick. The termination SiO_2 layer on top of the stack is tailored to be 127 nm thick. From design, the BSW propagation length is about 97 μm. Experimental measurements based on the Fourier-imaging systems described in Sec. 2.3 provide a lower limit for the BSW propagation length $L_{\mathrm{BSW}} = (\frac{\pi\sigma}{\lambda})^{-1} = 22\ \mu$m, where σ is the effective refractive index bandwidth of the BSW resonance dip,[31,32] with no corrections on the impulse response function of the imaging system.

The metasurface is made of gold nanorods periodically arranged in concentric rings or spirals, with an angular orientation that scales linearly by steps of $\Delta\psi = -60$ deg along the (outward) radial direction (see the inset in Fig. 1). The period in the radial direction is $\Lambda_g = 320$ m and the nanorod lateral size is 95 nm × 290 nm, with a 60 nm thickness. In the model, the number of periods is set to 12. The topological charge of the structure is set by taking a set of nanorod rings and introducing an azimuthal phase delay that translates into a radial displacement of nanorods belonging to each given ring, based on the following equation:

$$r = r_0 + \frac{M\theta}{k_{\mathrm{BSW}}},$$

where r_0 is the reference radius for each given ring (for example, $r_0 = 2.5\ \mu$m for the inner radius), k_{BSW} is the BSW wavevector, M is the metasurface topological charge, and θ is the angular position of a generic nanorod along the spiral. For example, in Fig. 1, a metasurface with negative topological charge is displayed.

Two electric dipoles are placed 10 nm above the multilayer surface, at the center of the axis-symmetric metasurface. Dipoles are parallel with the x-axis and y-axis, respectively. To simulate a rotating field for BSW coupling, the phase of the y-aligned dipole is delayed by $\pm\frac{\pi}{2}$ with respect to the x-aligned dipole. A near-field frequency-domain monitor for $\lambda = 520$ nm is placed 450 nm above the top 1DPC surface (in air), whereas a disk-shaped beam-blocker made of perfect electric conductor (PEC) is placed 20 nm below the monitor to avoid the detection of the source radiation directly emitted in free space (air), with

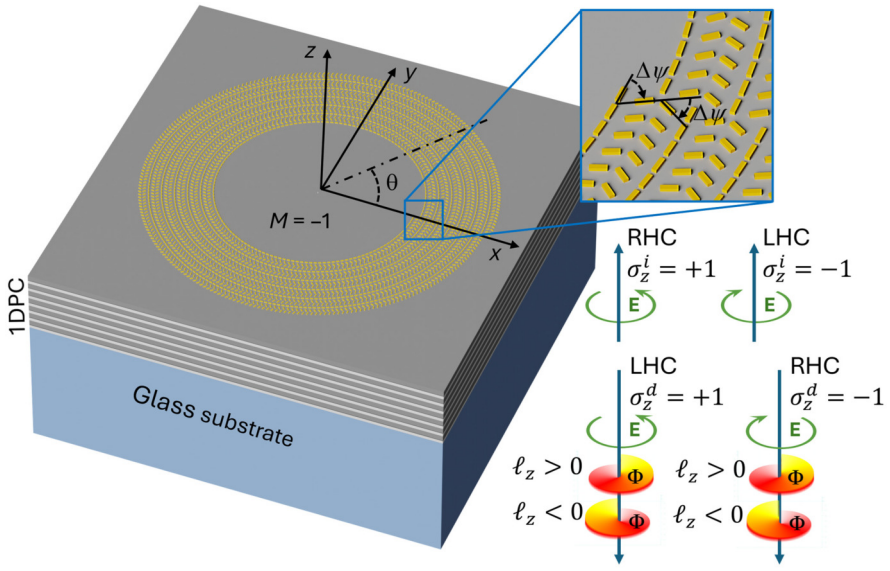

Fig. 1 Geometry of the computational model and reference system employed. In addition, conventions for values and signs of σ_z and ℓ_z related to incident and back-diffracted beams are indicated.

no BSW coupling. The beam-blocker radius is set to half the metasurface central spacer radius.

Far-field projections obtained from the near fields are then polarization-analyzed. All simulations were performed with ANSYS Lumerical (FDTD package).

2.2 Structure Fabrication

The 1DPC is made of a stack of alternating Ta_2O_5 and SiO_2 layers deposited on a glass substrate (150 μm thick) by plasma ion-assisted deposition under high vacuum conditions (APS904 coating system, Leybold Optics, Alzenau, Germany).

The metasurface was fabricated via a standard lift-off process. It should be specified that the fabricated metasurfaces had the same characteristics as the computational model, with the number of metasurface periods increased to 18 and the inner radius r_0 increased to 7.5 μm. A larger number of metasurface periods results in a smaller divergence and higher intensity of the diffracted OAM beam. A larger inner radius alleviates the chance of a direct illumination of the metasurface from the sidelobes of the focused beam. However, a longer-radial-propagation path for BSW before being diffracted implies a slight power loss because of leakage. The as-prepared 1DPC chip was first treated with a 2-min O_2 plasma to improve surface cleanliness and enhance resist adhesion. A diluted positive photoresist (AR-P 672, Allresist GmbH, Germany) was then spin-coated using a Laurell WS-650MZ-8NPPB spin coater (Lansdale, PA, USA) at 3000 r/min for 60 s, followed by a soft bake on a 150°C hot plate for 3 min.

Subsequently, a 30 nm-thick copper conductive layer was deposited onto the resist using a Q300T T Plus coater (Quorum, UK). The metasurface patterns were defined in the resist by electron beam lithography (EBL) using a Vistec EBPG5000 +HR system (Dortmund, Germany) operated at an acceleration voltage of 100 kV and an exposure dose of 900 $\mu C/cm^2$. After exposure, the copper layer was removed by immersing the chip in a diluted HNO_3 solution for 30 s, followed by rinsing with deionized (DI) water. Development was performed in an isopropanol/methyl isobutyl ketone solution (IPA:MIBK, 3:1 by volume) for 60 s, followed by a 30 s rinse in pure isopropanol to stop development and a final rinse with DI water.

The patterned chip was then coated with a 1 nm chromium adhesion layer, followed by thermal deposition of a 60 nm gold layer using a MiniLab STO26A R&D Magnetron Sputtering and thermal evaporation system (Moorfield Nanotechnology, UK). After deposition, the chip was soaked in acetone overnight to lift off the unwanted metal. The remaining photoresist was removed by gentle agitation and 5 s of sonication. Finally, the chip was rinsed with IPA and DI water and dried under a nitrogen gas flow. Examples of chiral metasurfaces with different topological charges are presented in Fig. 2(a).

2.3 Experimental Setup

1DPC decorated with chiral metasurfaces are experimentally investigated by means of a customized leakage radiation microscope[33–35] equipped with a spatial light modulator (SLM) and optical means to image the back focal plane (BFP) of the collecting objective. A sketch of the setup is presented in Fig. 2(b). A continuous-wave (CW) diode laser source pigtailed with a single mode fiber ($\lambda = 520$ nm, 2 nm spectral width, from Integrated Optics) is expanded, polarization-filtered, and sent onto a phase-only SLM (Pluto-2.1, Holoeye, Berlin, Germany). SLM is controlled in such a way that the -1th diffraction order produces a ring-shaped intensity distribution when focused onto the BFP of the imaging objective. Such a ring-shaped intensity is proportional to the Fourier transform squared amplitude of a Bessel beam, which is obtained from the SLM fed with a parabolic phase profile (mimicking a synthetic lens) superposed to the phase profile of a diffracting axicon. The 0th diffraction order is then spatially filtered out.[36] By properly adjusting the parabolic phase profile with the position of the external lens along the optical axis in the setup, size and divergence of the ring

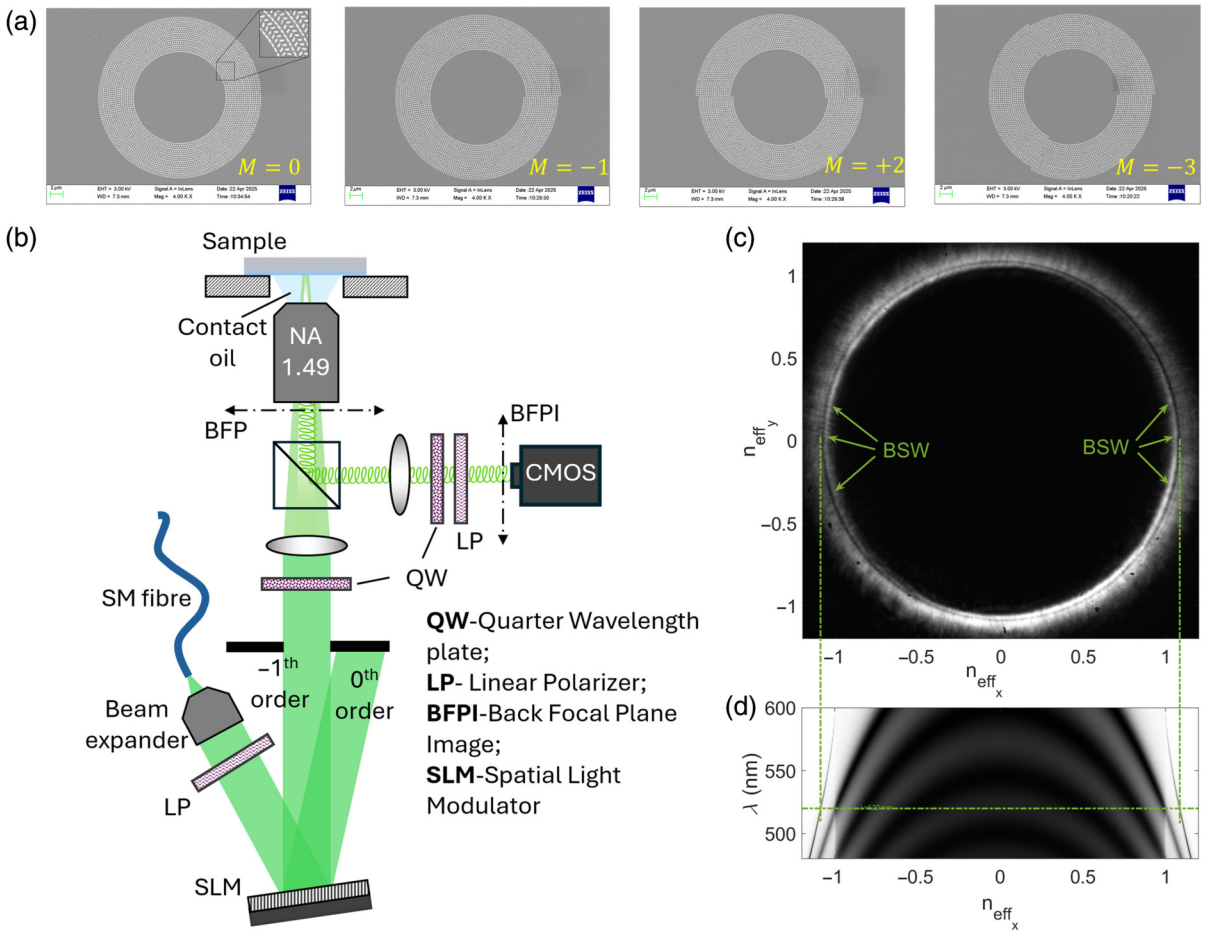

Fig. 2 (a) Scanning electron microscope (SEM) images of fabricated chiral metasurfaces with different topological charges. (b) Sketch of the experimental setup based on a leakage radiation microscope. QW—quarter wavelength plate; LP—linear polarizer; BFPI—back focal plane image; SLM—spatial light modulator. (c) BFP image of the reflected light at $\lambda = 520$ nm, distributed as a ring-shaped pattern created by means of the SLM. Illumination polarization is circular. The bright ring is crossed by a narrow, low-reflectivity belt, indicating phase-matching for BSW coupling at $\lambda = 520$ nm. (d) Calculated TE-polarized, spectrally-resolved reflectivity of the flat 1DPC, showing band structure of the crystal and the BSW dispersion.

pattern projected onto the objective BFP can be varied.[37,38] The imaging objective is a NA = 1.49 oil-immersion objective used for both illumination and collection in reflection mode. The illumination ring has a transverse size set to match the coupling condition for BSW (at the laser wavelength) and divergence such that the focused spot on the sample is well confined within the flat central area of the metasurface. This approach also offers the possibility to inscribe additional phase profiles onto the incident beam.[39] In Fig. 2(c), the BFP image of reflected light from a flat 1DPC is presented, showing the angular distribution of the illumination ring pattern, which is circularly polarized in this case. The dark circular belt crossing the bright ring indicates low reflected intensity, which corresponds to BSW coupling. This observation can be better understood when viewed alongside the reflectivity map $R(n_{\mathrm{eff}_x}, \lambda)$ of the 1DPC, calculated by assuming a TE-polarized illumination from the glass substrate at different incident angles θ_i and wavelength λ. Incident angles are considered in the xz-plane and $n_{\mathrm{eff}_x} = n_{\mathrm{glass}} \sin \theta_i$, where $n_{\mathrm{glass}} = 1.5$ is the refractive index of the glass substrate refractive. The objective NA = 1.49 allows illumination and collection within an angle $\theta_{\max}$, such as $n_{\mathrm{glass}} \sin \theta_{\max} = 1.49$. In Fig. 2(d), the band structure of the 1DPC is clearly visible as a modulation of reflected intensity. In particular, the narrow dark line running beyond the light line, i.e., at $n_{\mathrm{eff}_x} = 1$, and falling within a forbidden band (high-reflectivity region) of the 1DPC indicates the BSW dispersion. At the operating wavelength $\lambda = 520$ nm, BSW coupling occurs at $n_{\mathrm{eff}_x} = 1.084$, which corresponds to the reflectivity dip in Fig. 2(c), as indicated. It is worth noting that the BSW reflectivity dip has an isotropic distribution because of the circular polarization used for illumination (to be compared, e.g., with the case of linear polarization illumination as in Ref. 40). The ring-shaped illumination angular pattern offers the possibility to detect and analyze the out-coupled radiation diffracted at low spatial frequencies, i.e., in the central area of the BFP, without being affected by the background of reflected light. However, some background can be introduced on purpose by properly controlling the illumination angular pattern through the SLM. It yields an interference pattern originating from the overlap of the diffracted and the reflected light, revealing the OAM out-coupled radiation.

3 Results

The mechanism underlying the creation of free-space OAM beams in the current platform is illustrated along three main subsequent steps: (i) coupling of BSW from a focused circularly polarized illumination, (ii) propagation of BSW on the 1DPC surface, and (iii) diffraction by the chiral metasurface. As outlined in a previous study,[41] BSWs coupled from a focused circularly-polarized beam are characterized by a double-spiral wavefront and a radial propagation direction. Keeping this in mind, illumination must be focused onto the central flat area surrounded by the chiral metasurface, avoiding the direct illumination of the metasurface itself. By keeping the BSW coupling region separated from the patterned region on the 1DPC surface, the resulting diffraction involves BSWs only and no direct illumination. In addition, the (radial) distance between the illuminated area and the diffracting metasurface should be small enough to keep the device compact and reduce losses due to leakage into the substrate during BSW propagation.

Assuming the paraxial approximation is valid in the far field, the OAM, i.e., the vortex charge, of the BSW-assisted diffracted beam can be predicted considering the conservation of the z-component of the total angular momentum of light described as

$$J_z = \sigma_z^{\mathrm{i}} + M = \sigma_z^{\mathrm{d}} + \ell_z, \tag{1}$$

where σ_z^{i} and σ_z^{d} are the z-components of the SAM referred to the incident and diffracted radiation, respectively; M is the topological charge of the chiral metasurface; and ℓ_z is the vortex charge of the diffracted beam.[41] According to the geometry set in Fig. 1, it is worth noting that the incident right-hand circularly (RHC) and left-hand circularly (LHC) polarized beams (propagating in the positive z-axis) possess $\sigma_z^i = +1$ and $\sigma_z^i = -1$, respectively, whereas diffracted RHC and LHC polarized beams (propagating in the negative z-axis) have $\sigma_z^d = -1$ and $\sigma_z^d = +1$, respectively. In other words, σ_z is related to the sense of rotation of the electric field with respect to the reference system chosen. The same convention applies to ℓ_z, when looking at the spiral wavefront.

As apparent from Eq. (1), for given pairs σ_z^{i} and M, two possible solutions for ℓ_z are possible, corresponding to either RHC- or LHC-polarized diffracted beams. Figure 3 summarizes the different OAM values that can be obtained from diffraction by $-3 \le M \le +3$ metasurface, with either RHC ($\sigma_z^{\mathrm{i}} = +1$) or LHC ($\sigma_z^{\mathrm{i}} = -1$) incident illumination. Green boxes refer to diffracted beams with RHC ($\sigma_z^{\mathrm{d}} = -1$) polarization, whereas blue boxes refer to LHC ($\sigma_z^{\mathrm{d}} = +1$) polarization.

To reduce the (partial) spatial/angular overlap of two beams with different OAM and orthogonal (circular) polarization states,[41] chirality in the diffracting metasurface is introduced. As illustrated below, by introducing single scatterers with specific orientations, one polarization state (either RHC or LHC) of the diffracted light can be suppressed in favor of the other one. In the following, we will show results related to chiral metasurface wherein out-coupled radiation is substantially LHC-polarized, i.e., $\sigma_z^{\mathrm{d}} = +1$. That means that OAM beams resulting from combinations in blue boxes in Fig. 3 will be enabled, while those in green boxes will be frustrated, as demonstrated in the following.

3.1 Polarization-sensitive Diffracting Metasurface

In seminal works by Huang et al.,[42,43] chiral diffractive gratings capable of generating anomalous diffraction behavior were proposed. Such structures are made of nanorod antennas able to provide additional phase control leading to anomalous diffraction orders possessing opposite circular polarization with respect to the incident one. More specifically, when considering anomalous diffraction, the grating vector of the structure can be expressed as

$$G^{(m,\sigma_z)} = m\frac{2\pi}{\Lambda_g} + \sigma_z \frac{2\Delta\psi}{\Lambda_g}, \tag{2}$$

where m is the diffraction order, Λ_g is the grating spatial period, $\Delta\psi$ is the rotation angle between adjacent nanorods along the outward radial direction, and σ_z is the SAM z-component of the incident field. However, as in our case, the incident radiation is constituted by TE-polarized BSWs with no well-defined σ_z value, we translate the BSW out-coupling process into a BSW in-coupling from free-space circularly polarized radiation normally incident on the metasurface. If in-coupling occurs at $m = +1$ diffraction order, then $k_{\mathrm{d}}^{(+1,\sigma_z)} = k_{\mathrm{inc}}^{(\sigma_z)} + G^{(+1,\sigma_z)}$, where $k_{\mathrm{d}}^{(+1,\sigma_z)} = k_{\mathrm{BSW}}$ and $k_{\mathrm{inc}}^{(\sigma_z)} = 0$ are the transverse components of the wavevectors of the $m = +1$ diffracted radiation and

Diffracted OAM ℓ_z										
-5	-4	-3	-2	-1	0	$+1$	$+2$	$+3$	$+4$	$+5$
$\sigma_z^{\mathrm{i}} = -1$ $M = -3$	$\sigma_z^{\mathrm{i}} = -1$ $M = -2$	$\sigma_z^{\mathrm{i}} = -1$ $M = -3$	$\sigma_z^{\mathrm{i}} = -1$ $M = -2$	$\sigma_z^{\mathrm{i}} = +1$ $M = -3$	$\sigma_z^{\mathrm{i}} = +1$ $M = -2$	$\sigma_z^{\mathrm{i}} = -1$ $M = +3$	$\sigma_z^{\mathrm{i}} = +1$ $M = +2$	$\sigma_z^{\mathrm{i}} = +1$ $M = +3$	$\sigma_z^{\mathrm{i}} = +1$ $M = +2$	$\sigma_z^{\mathrm{i}} = +1$ $M = +3$
		$\sigma_z^{\mathrm{i}} = +1$ $M = -3$	$\sigma_z^{\mathrm{i}} = +1$ $M = -2$	$\sigma_z^{\mathrm{i}} = -1$ $M = -1$	$\sigma_z^{\mathrm{i}} = -1$ $M = +2$	$\sigma_z^{\mathrm{i}} = +1$ $M = +1$	$\sigma_z^{\mathrm{i}} = -1$ $M = +2$	$\sigma_z^{\mathrm{i}} = -1$ $M = +3$		
		$\sigma_z^{\mathrm{i}} = -1$ $M = -1$	$\sigma_z^{\mathrm{i}} = -1$ $M = 0$	$\sigma_z^{\mathrm{i}} = +1$ $M = -1$	$\sigma_z^{\mathrm{i}} = +1$ $M = 0$	$\sigma_z^{\mathrm{i}} = -1$ $M = +1$	$\sigma_z^{\mathrm{i}} = +1$ $M = 0$	$\sigma_z^{\mathrm{i}} = +1$ $M = +1$		
				$\sigma_z^{\mathrm{i}} = -1$ $M = +1$	$\sigma_z^{\mathrm{i}} = -1$ $M = 0$	$\sigma_z^{\mathrm{i}} = +1$ $M = -1$				
	$\sigma_z^{\mathrm{d}} = +1$ - enabled									
	$\sigma_z^{\mathrm{d}} = -1$ - frustrated									

Fig. 3 Diffracted beams with polarization $\sigma_z^{\mathrm{d}} = \pm 1$ and OAM ℓ_z as produced by metasurfaces having topological charges M, with incident polarization $\sigma_z^{\mathrm{i}} = \pm 1$.

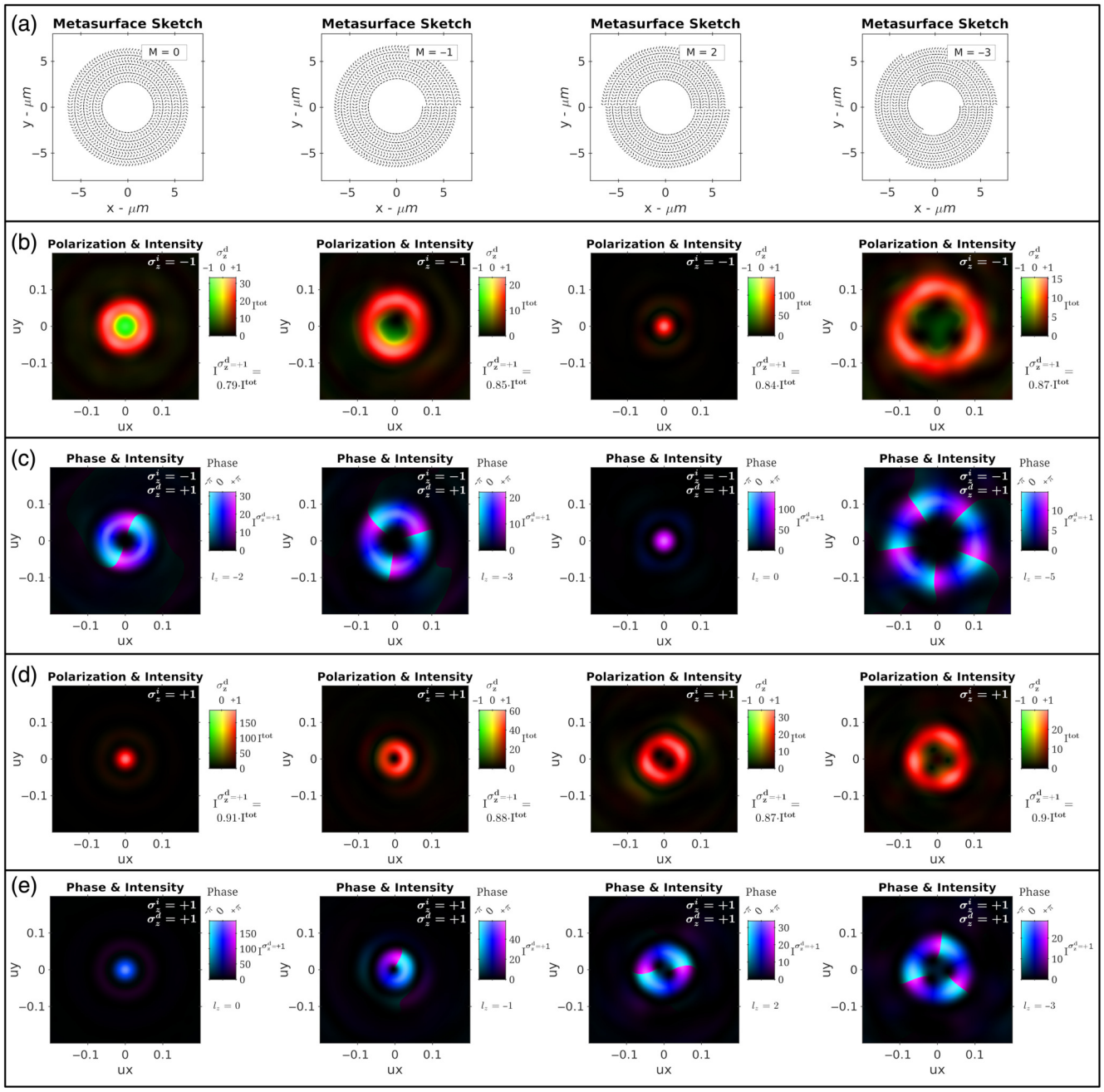

Fig. 4 Simulation results for the metasurfaces with four different topological charges. Results relate to far-field projections of calculated near-fields and are displayed using a bidimensional HSV colormap, where the hue encodes one physical quantity (either polarization state or phase) and the saturation/value encodes another physical quantity (either total intensity or intensity related to $\sigma_z^{\mathrm{d}} = +1$ polarization). In particular: row (a): sketches of the considered metasurfaces; row (b): total intensity $I^{\mathrm{tot}} = I^{\sigma_z^{\mathrm{d}}=+1} + I^{\sigma_z^{\mathrm{d}}=-1}$ and polarization state of the diffracted field for an input rotating field with $\sigma_z^i = -1$. The hue encodes the polarization state, whereas the saturation/value encodes I^{tot}. Power fraction carried by $I^{\sigma_z^{\mathrm{d}}=+1}$ is also indicated; row (c): intensity $I^{\sigma_z^{\mathrm{d}}=+1}$ and phase of the preferentially diffracted circular polarization $\sigma_z^d = +1$, for an input rotating field with $\sigma_z^i = -1$: the hue encodes the phase of the field, while the saturation/value encodes the intensity $I^{\sigma_z^{\mathrm{d}}=+1}$; row (d): total intensity I^{tot} and polarization state of the diffracted field for an input rotating field with $\sigma_z^i = +1$; row (e): intensity $I^{\sigma_z^{\mathrm{d}}=+1}$ and phase of the preferentially diffracted circular polarization $\sigma_z^d = +1$, for an input rotating field with $\sigma_z^i = +1$.

the incident radiation, respectively. As a result, the grating period is

$$\Lambda_g = \frac{2\pi}{k_{\mathrm{BSW}}}\left(1 + \frac{\sigma_z \Delta\psi}{\pi}\right). \tag{3}$$

If, for example, BSW is expected to be in-coupled with $\sigma_z = +1$ incident polarization, we obtain several possible solutions for the grating period, depending on $\Delta\psi$. After choosing $\Delta\psi = -\frac{\pi}{3}$, the grating period is $\Lambda_g = \frac{4\pi}{3k_{\mathrm{BSW}}} < \frac{2\pi}{k_{\mathrm{BSW}}}$, which leads to a remarkable result: for $\sigma_z = +1$ incident radiation, $k_{\mathrm{d}}^{(+1,+1)} = k_{\mathrm{BSW}}$, whereas for $\sigma_z = -1$ incident radiation, $k_{\mathrm{d}}^{(+1,-1)} = 0 + \frac{2\pi}{\Lambda_g} - \frac{2\Delta\psi}{\Lambda_g} = 2k_{\mathrm{BSW}}$. The advantage of this configuration is clear in BSW out-coupling. In fact, the $m = -1$ diffraction order from an incident BSW can be written as

$$k_{\mathrm{d}}^{(-1,\sigma_z)} = k_{\mathrm{BSW}} - \frac{2\pi}{\Lambda_g} + \sigma_z \frac{2\Delta\psi}{\Lambda_g} = k_{\mathrm{BSW}} - \frac{3}{2}k_{\mathrm{BSW}} - \sigma_z \frac{1}{2}k_{\mathrm{BSW}}, \tag{4}$$

which leads to $k_d^{(-1,\sigma_z)} = 0$ for $\sigma_z = -1$ and $k_d^{(-1,\sigma_z)} = -k_{\mathrm{BSW}}$ for $\sigma_z = +1$. Keeping in mind that σ_z in Eq. (4) refers to the incident polarization and anomalous diffraction inverts the circular polarization state, we can conclude that BSWs are normally out-coupled in free space with polarization $\sigma_z = +1$, whereas $\sigma_z = -1$ polarization is diffracted as back-reflected BSWs, as in a distributed Bragg reflector used in cavities.[44–46] At the operating wavelength $\lambda = 520$ nm, $k_{\mathrm{BSW}} = \frac{2\pi}{\lambda} \cdot n_{\mathrm{eff}} \cong 13.1\ \mu\mathrm{m}^{-1}$, and the grating period is $\Lambda_g \cong 320$ nm. By arranging the chiral nanorod geometry in circular rings or spiral arms and leveraging the topological charge of the metasurface, it is then possible to impart an additional geometrical phase to the polarization-selected diffracted beam, as summarized in Fig. 3. The expected polarization selectivity favoring, $\sigma_z^d = +1$, is confirmed by the computational model developed (Fig. 4).

Far field diffraction patterns obtained from clockwise (mimicking $\sigma_z^{\mathrm{i}} = -1$ incident light) and counter-clockwise (mimicking $\sigma_z^{\mathrm{i}} = +1$ incident light) rotating dipoles on the 1DPC surface (see Sec. 2) are calculated for metasurfaces with topological charges $M = 0, -1, +2$, and -3; [Fig. 4(a)]. According to the reference system adopted here, far-field intensities related to $\sigma_z^{\mathrm{d}} = +1$ and $\sigma_z^{\mathrm{d}} = -1$ polarization are named $I^{\sigma_z^{\mathrm{d}}=+1}$ and $I^{\sigma_z^{\mathrm{d}}=-1}$, respectively. In Figs. 4(b) and 4(d), the total intensity $I^{\mathrm{tot}} = I^{\sigma_z^{\mathrm{d}}=+1} + I^{\sigma_z^{\mathrm{d}}=-1}$ is plotted as saturation values, whereas the hue (green to red) in the false color images encodes the polarization state defined as $\frac{I^{\sigma_z^{\mathrm{d}}=+1} - I^{\sigma_z^{\mathrm{d}}=-1}}{I^{\sigma_z^{\mathrm{d}}=+1} + I^{\sigma_z^{\mathrm{d}}=-1}}$, equivalent to S_3/S_0 if Stokes parameters are used. As seen, for all considered configurations, $\sigma_z^{\mathrm{d}} = +1$ circular polarization carries the major fraction of the overall diffracted power, from 78.9% to 90.6%, depending on the case. In addition, the phase of the diffraction patterns presented in Figs. 4(c) and 4(e) confirms the OAM values as expected from calculations from Fig. 3. Diffraction patterns from metasurfaces with other topological charges are illustrated in Fig. S1 in the Supplementary Material.

As discussed above, the metasurface design is based on the knowledge of the BSW effective index at the desired operation wavelength. In case of deviations of the BSW effective index within a range from 1.06 to 1.12 (because of fabrication errors in the 1DPC layer thickness), OAM beams are still obtained, with variation in polarization selectivity $\frac{I^{\sigma_z^{\mathrm{d}}=+1}}{I^{\sigma_z^{\mathrm{d}}=+1} + I^{\sigma_z^{\mathrm{d}}=-1}}$ not exceeding 5%.

3.2 Experimental Measurements

In a previous study, it has been shown that TE-polarized BSW coupled on a flat multilayer through a high-NA focused beam possesses a double-spiral wavefront while propagating radially from the coupling spot.[41] The helicity of the BSW wavefront depends on the handedness of the incident circular polarization as a result of spin-orbit coupling.[47] According to Fig. 3, OAM beams with different vortex charges ℓ_z can be obtained by

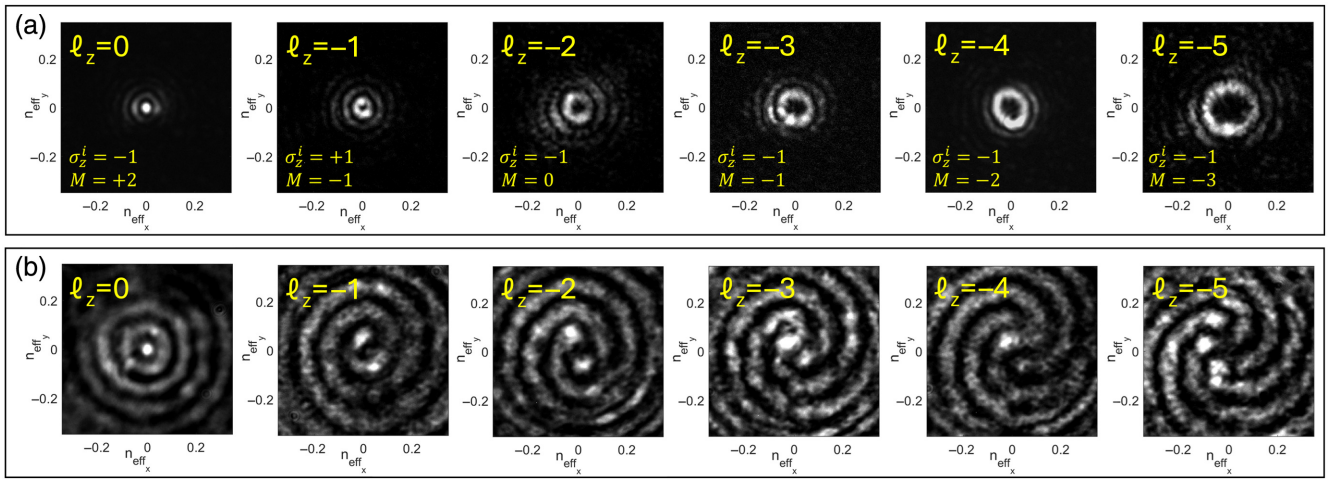

Fig. 5 (a) Back focal plane intensity patterns and (b) corresponding interferograms of diffracted beams resulting from different combinations of incident polarization ($\sigma_z^{\mathrm{i}} = \pm 1$) and metasurface topological charges (M). The vortex charge ℓ_z of the diffracted beams can be appreciated by the number of spiral interference fringes appearing in the interferograms. Collection polarization is $\sigma_z^{\mathrm{d}} = +1$.

means of several combinations of incident SAM σ_z^{i} and metasurface topological charge M. In Fig. 5(a), an illustrative set of far-field intensity patterns related to OAM beams with $-5 \leq \ell_z \leq 0$ is displayed. Although all intensity patterns are collected with $\sigma_z^{\mathrm{d}} = +1$ polarization (because $\sigma_z^{\mathrm{d}} = -1$ is frustrated), the incident polarization can be either left- or right-handed. It's worth noting that the diffracted beam divergence increases with $|\ell_z|$, as expected, with the corresponding NA always being smaller than 0.15. The vortex charge can be visualized by allowing some reflected background light to be superposed with the diffracted OAM beam and leveraging interference between the helical wavefront of the OAM beams and the converging parabolic wavefront of the background.[48] As a result, the number of fringes and their handedness are indicative of $|\ell_z|$ and $\mathrm{sgn}(\ell_z)$, respectively. In Supplementary Videos 1 and 2, OAM beams with varying vortex charges are shown while smoothly changing the incident polarization state.

Polarization selectivity is demonstrated in Figs. 6(a) and 6(b), where a direct comparison of illustrative detected intensity patterns polarization-filtered with $\sigma_z^{\mathrm{d}} = +1$ and $\sigma_z^{\mathrm{d}} = -1$ is shown.

In both cases, regardless of the incident polarization employed [$\sigma_z^{\mathrm{i}} = -1$ for $M = -1$ structure in Fig. 6(a) and $\sigma_z^{\mathrm{i}} = +1$ for $M = 0$ structure in Fig. 6(b)], the detected intensity at $\sigma_z^{\mathrm{d}} = -1$ is much weaker with respect to $\sigma_z^{\mathrm{d}} = +1$. More specifically, for the case in Fig. 6(a), after integration of the detected intensities $I^{\sigma_z^{\mathrm{d}}=-1}$ and $I^{\sigma_z^{\mathrm{d}}=+1}$ within NA < 0.1, we found a polarization selectivity $\frac{I^{\sigma_z^{\mathrm{d}}=+1}}{I^{\sigma_z^{\mathrm{d}}=-1}+I^{\sigma_z^{\mathrm{d}}=+1}} = 0.74$ (84.9% from the computational model). For the case in Fig. 6(b), the polarization selectivity is 0.79 (90.6% from the computational model). A further demonstration of the efficacy of the polarization selectivity is provided in Supplementary Video 3. There, a time sequence is shown wherein the collection of the diffracted intensity from a $M = -1$ metasurface is observed to significantly decrease while the collection polarization is gradually changed from $\sigma_z^{\mathrm{d}} = +1$ to $\sigma_z^{\mathrm{d}} = -1$.

As a last aspect to address, we demonstrate that diffraction effects described above are mediated by BSW coupling and not due to direct illumination of the metasurface with the incident beam. By operating on the SLM, we were able to detect the back focal plane diffraction pattern while changing the radius of the illumination ring. In the image sequence presented in Fig. 7, the incident beam has a ring-shaped angular spectrum distribution such that the transverse wave vector can be tuned to match the BSW wave vector. In particular, when the incident beam has transverse wave vectors larger than k_{BSW} [Fig. 7(a)], only some residual diffracted intensity (through ordinary diffraction) can be observed at small angles with respect to the optical axis, i.e., at the BFP center. Similarly, when the incident wavevectors are smaller than k_{BSW} [Fig. 7(c)], negligible diffraction is detected. Instead, when the incident wavevectors are matched to BSWs when coupling occurs, the well-known OAM beam is clearly observed ($\ell_z = -3$). The full-time sequence can be seen in Supplementary Video 4, wherein the illumination ring diameter is smoothly varied.

4 Conclusion

A dielectric multilayer platform sustaining TE-polarized BSWs has been decorated with a diffractive chiral metasurface made of gold nanorods. When BSWs are coupled with a focused circularly polarized beam, the resulting OAM diffraction patterns are observed in the far-field, with an angular divergence corresponding to an NA < 0.15, depending on the vortex charge. In addition, the observed OAM beams show a circular polarization selectivity larger than 74%, estimated on the overall diffracted intensity. The proposed approach is suitable for integration with single sources, provided a deterministic positioning of the emitters within specific locations on the metasurface, which nowadays represents the most technologically challenging task.[19,49] Potentially advantageous techniques to overcome such a key limitation include the direct printing of colloidal quantum dots by means of electrostatic autofocusing systems.[50] Using an underlying 1DPC allows leveraging other optical functions related to the arrangement of forbidden bands, for example, to facilitate/inhibit transmission at given wavelengths or propagation angles. In fact, as mode-assisted emission from individual sources within photonic or plasmonic nanostructures is concerned, a known issue is represented by diffraction occurring in both air and substrate media, thus hampering an efficient use of emitted power, particularly critical in the single-photon regime. In plasmonic structures, this limitation can be overcome using thick metallic, reflective coatings,[51] at the cost of some absorption losses. In our case, high-reflectance bands can be engineered at desired angles/wavelengths so that emission can be significantly suppressed in the substrate, as demonstrated for fluorescence-based biosensing platforms using BSWs.[52]

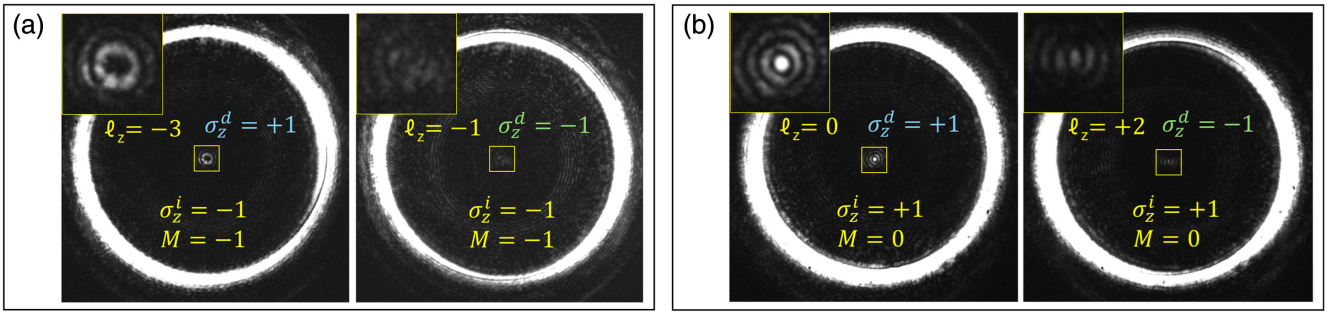

Fig. 6 Examples of polarization selectivity. (a) Back focal plane diffraction patterns from $M = -1$ metasurface, with BSW coupled from $\sigma_z^{\mathrm{i}} = -1$ incident light and polarization-filtered in collection with either $\sigma_z^{\mathrm{d}} = +1$ (left) or $\sigma_z^{\mathrm{d}} = -1$ (right); (b) is the same as in (a) but with $M = 0$ metasurface and $\sigma_z^{\mathrm{i}} = +1$. Magnified views of the diffracted patterns at the center of the back focal plane are shown in the insets.

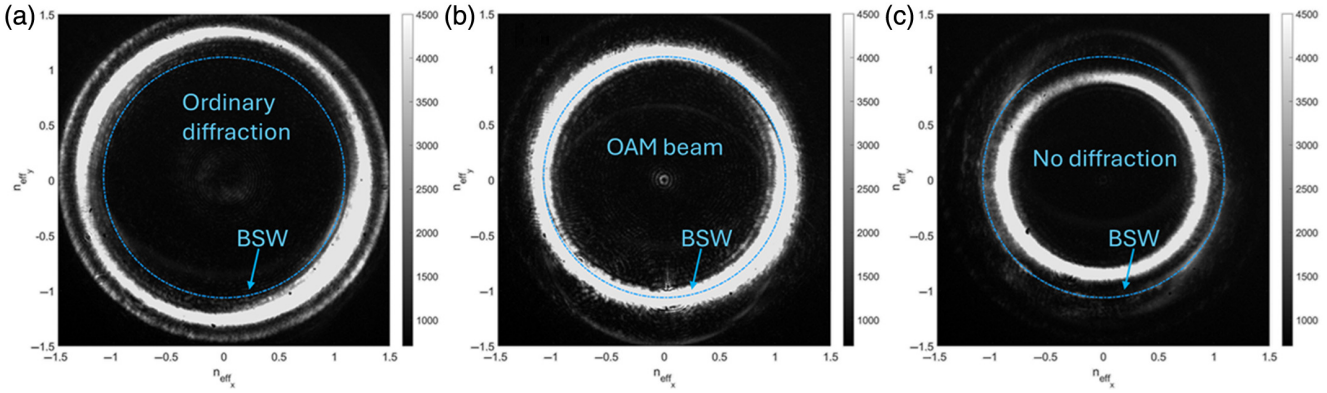

Fig. 7 Dependence of diffraction on BSW coupling. In (a) and (c), the angular spectrum of the illuminating beam is such that no BSWs are coupled because the phase-matching condition for the transverse wavevector is not matched. In particular, the transverse wavevector of the incident beam is larger in (a) and smaller in (c) as compared with the BSW wavevector (dotted cyan circle). In (b), the incident beam couples to BSW, and the corresponding diffraction pattern appears close to the optical axis. In this case, illumination has $\sigma_z^{\mathrm{i}} = -1$, collected light has $\sigma_z^{\mathrm{d}} = +1$, and the metasurface has $M = -1$ topological charge.

5 Appendix: Supplemental Videos

Video 1 Metasurface with topological charge $M = -3$ illuminated with an incident beam having circular polarization varying from $\sigma_z^i = -1$ to $\sigma_z^i = +1$, producing OAM beams moving from $\ell_z = -5$ to $\ell_z = -3$. Detected intensity has $\sigma_z^d = +1$ (MP4, 1.16 MB [URL: https://doi.org/10.1117/1.APN.5.2.026008.s1]).

Video 2 Metasurface with topological charge $M = -1$ illuminated with an incident beam having circular polarization varying from $\sigma_z^i = -1$ to $\sigma_z^i = +1$, producing OAM beams moving from $\ell_z = -3$ to $\ell_z = -1$. Detected intensity has $\sigma_z^d = +1$ (MP4, 516 KB [URL: https://doi.org/10.1117/1.APN.5.2.026008.s2]).

Video 3 Metasurface with topological charge $M = -1$ illuminated with an incident beam having circular polarization $\sigma_z^i = +1$. In collection, polarization is changing from $\sigma_z^d = +1$ to $\sigma_z^d = -1$, resulting in a clear fading of the detected pattern (MP4, 884 KB [URL: https://doi.org/10.1117/1.APN.5.2.026008.s3]).

Video 4 Dependence of diffraction on BSW coupling. The size of the illumination rings is smoothly varied in the transverse wavevector space, and so is the coupling of BSW. Diffracted OAM beams appear only when BSWs are coupled. Illumination has $\sigma_z^{\mathrm{i}} = -1$, collected light has $\sigma_z^{\mathrm{d}} = +1$, and the metasurface has $M = -1$ topological charge (MP4, 4.77 MB [URL: https://doi.org/10.1117/1.APN.5.2.026008.s4]).

Disclosures

The authors declare no conflicts of interest.

Code and Data Availability

The data that support the findings of this study are available from the last author, E. Descrovi, upon reasonable request at emiliano.descrovi@polito.it.

Acknowledgments

This work was supported by the project RAVEN from the European Union's Horizon Europe Research and Innovation Programme (Grant No. 101135787), the French Agence Nationale de la Recherche under project CIFOM (Grant No. ANR-23-CE42-0021), the EIPHI Graduate School (Grant No. ANR-17-EURE-0002), and the Region Bourgogne Franche-Comte through the Dynastage fellowship and the Erasmus+ Programme of the European Union.

References

1. P. Coullet, L. Gil, and F. Rocca, "Optical vortices," *Opt. Commun.* **73**(5), 403–408 (1989).
2. L. Allen et al., "Orbital angular momentum of light and the transformation of Laguerre-Gaussian laser modes," *Phys. Rev. A* **45**(11), 8185–8189 (1992).
3. G. Molina-Terriza, J. P. Torres, and L. Torner, "Twisted photons," *Nat. Phys.* **3**(5), 305–310 (2007).
4. X. Wang et al., "Recent advances on optical vortex generation," *Nanophotonics* **7**(9), 1533–1556 (2018).
5. H. Rubinsztein-Dunlop, "Roadmap on structured light," *J. Opt.* **19**(1), 013001 (2017).
6. Y. Shen et al., "Optical vortices 30 years on: OAM manipulation from topological charge to multiple singularities," *Light Sci. Appl.* **8**, 90 (2019).
7. L. Marrucci, C. Manzo, and D. Paparo, "Optical spin-to-orbital angular momentum conversion in inhomogeneous anisotropic media," *Phys. Rev. Lett.* **96**(16), 163905 (2006).
8. J. Zhang et al., "An InP-based vortex beam emitter with monolithically integrated laser," *Nat. Commun.* **9**(1), 2652 (2018).
9. X. Cai et al., "Integrated compact optical vortex beam emitters," *Science* **338**(6105), 363–366 (2012).
10. K. G. Cognée et al., "Generation of pure OAM beams with a single state of polarization by antenna-decorated microdisk resonators," *ACS Photonics* **7**, 3049–3060 (2020).
11. Y. Wang et al., "Integrated photonic emitter with a wide switching range of orbital angular momentum modes," *Sci. Rep.* **6**(1), 22512 (2016).
12. G. Ruffato et al., "Holographic silicon metasurfaces for total angular momentum demultiplexing applications in telecom," *Appl. Sci.* **9**(11), 2387 (2019).

13. R. Chen et al., "Orbital angular momentum waves: generation, detection, and emerging applications," *IEEE Commun. Surv. Tut.* **22**(2), 840–868 (2020).
14. J. Lin et al., "Nanostructured holograms for broadband manipulation of vector beams," *Nano Lett.* **13**(9), 4269–4274 (2013).
15. Y.-Y. Xie, "Metasurface-integrated vertical cavity surface-emitting lasers for programmable directional lasing emissions," *Nat. Nanotechnol.* **15**, 125–130 (2020).
16. Z. Wang et al., "Induced optical chirality and circularly polarized emission from achiral CdSe/ZnS quantum dots via resonantly coupling with plasmonic chiral metasurfaces," *Laser Photonics Rev.* **13**(3), 1800276 (2019).
17. X. Liu et al., "On-chip generation of single-photon circularly polarized single-mode vortex beams," *Sci. Adv.* **9**(32), eadh0725 (2023).
18. S. I. Bozhevolnyi and N. A. Mortensen, "Plasmonics for emerging quantum technologies," *Nanophotonics* **6**(5), 1185–1188 (2017).
19. X. Liu et al., "Ultracompact single-photon sources of linearly polarized vortex beams," *Adv. Mater.* **36**(4), 2304495 (2024).
20. W. M. Robertson and M. S. May, "Surface electromagnetic wave excitation on one-dimensional photonic band-gap arrays," *Appl. Phys. Lett.* **74**(13), 1800–1802 (1999).
21. M. Ballarini et al., "A polymer-based functional pattern on one-dimensional photonic crystals for photon sorting of fluorescence radiation," *Opt. Express* **20**(6), 6703–6711 (2012).
22. M. Ballarini et al., "Bloch surface waves-controlled emission of organic dyes grafted on a one-dimensional photonic crystal," *Appl. Phys. Lett.* **99**(4), 043302 (2011).
23. M. Liscidini et al., "Strong modification of light emission from a dye monolayer via Bloch surface waves," *Opt. Lett.* **34**(15), 2318–2320 (2009).
24. A. Angelini et al., "Fluorescence diffraction assisted by Bloch surface waves on a one-dimensional photonic crystal," *New J. Phys.* **15**(7), 073002 (2013).
25. A. Angelini et al., "Surface-wave-assisted beaming of light radiation from localized sources," *ACS Photonics* **1**(7), 612–617 (2014).
26. A. Angelini et al., "Focusing and extraction of light mediated by Bloch surface waves," *Sci. Rep.* **4**(1), 5428 (2015).
27. B. Vosoughi Lahijani et al., "Centimeter-scale propagation of optical surface waves at visible wavelengths," *Adv. Opt. Mater.* **10**(10), 2102854 (2022).
28. E. Mogni et al., "One-dimensional photonic crystal for surface mode polarization control," *Adv. Opt. Mater.* **10**(21), 2200759 (2022).
29. A. Sinibaldi et al., "Combining label-free and fluorescence operation of Bloch surface wave optical sensors," *Opt. Lett.* **39**(10), 2947–2950 (2014).
30. T.-L. Guo et al., "Polarization-insensitive surface mode excitation on metamaterial-terminated one-dimensional photonic crystals," *J. Phys. Photonics* **7**(3), 035007 (2025).
31. R. Ulrich, "Theory of the Prism–Film coupler by plane-wave analysis," *J. Opt. Soc. Am.* **60**, 1337–1350 (1970).
32. E. Descrovi et al., "Near-field imaging of Bloch surface waves on silicon nitride one-dimensional photonic crystals," *Opt. Express* **16**(8), 5453–5464 (2008).
33. A. Drezet et al., "Leakage radiation microscopy of surface plasmon polaritons," *Mater. Sci. Eng.: B* **149**(3), 220–229 (2008).
34. D. G. Zhang, X. Yuan, and A. Bouhelier, "Direct image of surface-plasmon-coupled emission by leakage radiation microscopy," *Appl. Opt.* **49**(5), 875–879 (2010).
35. E. Descrovi et al., "Leakage radiation interference microscopy," *Opt. Lett.* **38**(17), 3374–3376 (2013).
36. A. Angelini, "Resonant evanescent complex fields on dielectric multilayers," *Opt. Lett.* **40**(24), 5746–5749 (2015).
37. S. N. Khonina et al., "Modern types of axicons: new functions and applications," *Sensors* **21**(19), 6690 (2021).
38. S. Hasegawa et al., "Diffraction-limited ring beam generated by radial grating," *OSA Contin.* **1**(2), 283 (2018).
39. D. Zhang et al., "Silver nanowires for reconfigurable Bloch surface waves," *ACS Nano* **11**(10), 10446–10451 (2017).
40. D. Zhang et al., "Back focal plane imaging of directional emission from dye molecules coupled to one-dimensional photonic crystals," *Nanotechnology* **25**(14), 145202 (2014).
41. U. Stella et al., "Vortex beam generation by spin-orbit interaction with Bloch surface waves," *ACS Photonics* **7**(3), 774–783 (2020).
42. L. Huang et al., "Dispersionless phase discontinuities for controlling light propagation," *Nano Lett.* **12**(11), 5750–5755 (2012).
43. L. Huang et al., "Helicity dependent directional surface plasmon polariton excitation using a metasurface with interfacial phase discontinuity," *Light Sci. Appl.* **2**(3), e70 (2013).
44. U. Stella et al., "Enhanced directional light emission assisted by resonant Bloch surface waves in circular cavities," *ACS Photonics* **6**(8), 2073–2082 (2019).
45. N. Marcucci et al., "Bloch surface waves in open Fabry–Perot microcavities," *Micromachines* **14**(3), 509 (2023).
46. T. Perani, D. Aurelio, and M. Liscidini, "Bloch-surface-wave photonic crystal nanobeam cavity," *Opt. Lett.* **44**(21), 5133–5136 (2019).
47. F. Feng et al., "Spin-orbit coupling controlled near-field propagation and focusing of Bloch surface wave," *Opt. Express* **27**(20), 027536 (2019).
48. M. S. Soskin et al., "Topological charge and angular momentum of light beams carrying optical vortices," *Phys. Rev. A* **56**(5), 4064–4075 (1997).
49. C. Frydendahl et al., "2D semiconductors as on-chip light sources for integrated nanophotonics," *Nano Lett.* **25**(16), 6414–6420 (2025).
50. P. Galliker et al., "Direct printing of nanostructures by electrostatic autofocussing of ink nanodroplets," *Nat. Commun.* **3**(1), 890 (2012).
51. Y. Deng et al., "Recent progress in metasurface-enabled optical waveplates," *Nanophotonics* **11**(10), 2219–2244 (2022).
52. K. Toma et al., "Bloch surface wave-enhanced fluorescence biosensor," *Biosens. Bioelectron.* **43**, 108–114 (2013).

Niccolò Marcucci is a postdoctoral researcher at the CNR—Istituto di Fisica Applicata Nello Carrara (IFAC), where he focuses on the modeling and fabrication of fiber optic sensors, including long-period gratings (LPGs) and fiber Bragg gratings (FBGs), for biomedical applications. He earned his PhD in experimental physics from Politecnico di Torino, with a thesis on Bloch surface waves on dielectric multilayers, combining numerical simulations, nanofabrication, and optical characterization.

Zongyuan Tang received his MS degree in materials engineering and nanotechnology from City University of Hong Kong, Hong Kong, China, in 2022. He is currently pursuing a joint PhD program between Politecnico di Torino, Torino, Italy and Southern University of Science and Technology, Shenzhen, China. His current research interests include Bloch surface waves and liquid crystal optics.

Thierry Grosjean is a senior scientist at the CNRS in France. He joined the CNRS in 2005 and conducts research at the FEMTO-ST Institute in the field of nanophotonics. His research focuses on light–matter interactions at the nanoscale, with particular emphasis on optical chirality and spin–orbit interactions (SOIs) in plasmonic nanostructures. This work includes pure magnetic spin-locking on Bloch surface waves, SOI-enabled directional plasmonic waveguiding on the nanoscale, and optically induced nanoscale magnetic fields leading, for example, to spectrally tunable spin-wave generation.

Matthieu Roussey is leading the integrated optics and sensing group (about 15 researchers) of the Center for Photonics Sciences at UEF in

Joensuu. He obtained his PhD from the FEMTO-ST institute (Besançon, France) in 2007. He was the team leader in the Optics & Photonics Technology Lab at EPFL (Neuchâtel, Switzerland) from 2007 to 2011. Since 2011, he has been working as a senior researcher at UEF, from which he obtained a tenure-track position in experimental photonics in October 2016. In October 2020, he obtained the position of full professor. His research topics include dielectric surface waves, novel platforms for integrated optics, complex integrated devices, and environmental monitoring.

Tian-Long Guo is a postdoctoral researcher at the University of Eastern Finland. He received his PhD in materials science and engineering from Northeastern University, China, in 2018, and his MSc degree in materials engineering and nanotechnology from City University of Hong Kong in 2010. His research focuses on nanophotonic devices, Bloch surface waves, and metamaterial-based light manipulation, with an emphasis on advanced micro-/nano-fabrication techniques.

Biographies for the other authors are not available.